Relationship between microstructure, and residual strain and stress in stainless steels in-situ alloyed by double-wire arc additive manufacturing (D-WAAM) process

Juliette Théodore, Laurent Couturier, Baptiste Girault, Sandra Cabeza, Thilo Pirling, Renaud Frapier, Grégoire Bazin, Bruno Courant

Essential title page information

Title: Relationship between microstructure, and residual strain and stress in stainless steels *in-situ* alloyed by Double-Wire Arc Additive Manufacturing (D-WAAM) process

Author names and affiliations: Juliette Théodore[a,b,c], Laurent Couturier[b], Baptiste Girault[c], Sandra Cabeza[d], Thilo Pirling[d], Renaud Frapier[e], Grégoire Bazin[a], Bruno Courant[c]

[a] Nantes Université, IRT Jules Verne, F-44000 Nantes, France

[b] Nantes Université, CNRS, Institut des Matériaux de Nantes Jean Rouxel, IMN, F-44000 Nantes, France

[c] Nantes Université, École Centrale Nantes, CNRS, GeM, UMR 6183, F-44600 Saint-Nazaire, France

[d] Institut Laue-Langevin, 71 Avenues des Martyrs, F-38000 Grenoble, France

[e] Mat-In-Meca, Le Gué, F-85110 Sainte-Cécile, France

Corresponding author: juliette.theodore@gmail.com

Keywords (6 max)

Double-Wire Arc Additive Manufacturing, Tungsten Inert Gas, Stainless steel, Residual stress, Residual strain, Microstructure

Abstract

In the field of welding, assembly of thick parts requires the base metal to be chamfered, followed by multipass welding as additive manufacturing processes require the layering of deposits. In both cases, the process generates thermal, mechanical, and metallurgical phenomena resulting in the formation of residual strains and stresses. Strains must be limited, as they can cause misalignments during welding and leads to geometrical defects. Residual stresses are especially problematic in structural assemblies, as they add to the external stresses applied to the part during service, often reducing its in-service lifetime and increasing the risk of failure.

The objective of this study is to use two stainless steel filler metals with different coefficients of thermal expansion (austenitic 304L and ferritic 430) to reduce the distribution of residual stresses and strains in the context of deposits produced by the Double-Wire Arc Additive Manufacturing process on 304L stainless steel baseplates. To achieve such a goal, the two filler metals are mixed in various proportions. Residual stresses are determined using neutron diffraction and contour method. Strains are studied with profilometry. Microstructure is analyzed via EBSD, free dilatometry tests and XRD.

We were able to reduce strains and stresses with a three-phase microstructure (austenite, ferrite, and martensite). The part that offers the best compromise (50% 430 - 50% 304L) exhibits a 67% reduction in strain, and stresses are reduced down to 40%. The results obtained from neutron diffraction and contour method exhibit a close agreement, with a discrepancy standing below 100 MPa.

1 Introduction

Welding consists in assembling two parts or more, thanks to a heat source or a mechanical load, with or without filler metal, to form a mechanical and metallurgical continuity. Tungsten Inert Gas (TIG) process is one of the multiple processes commonly used to weld metals. This process is widely used since it is suitable for most alloys, simple to use, and known to perform accurate, aesthetic, and proper welds. In addition, it produces very little fumes, enables welding in any position, and is very versatile since it can be used for welding with or without filler metal. It can be easily automated which enables to increase productivity and improves not only the reproducibility and quality of the welds but also the working conditions for the welders [1].

TIG process is also suitable to weld a wide range of work piece thicknesses. However, the assembly of thick parts (baseplates or tubes) requires a chamfering followed by multipass welding that generates a succession of thermal cycles, alternating heating and cooling steps. These operations lead to thermal, mechanical, and metallurgical phenomena responsible for the formation of high residual strains and stresses [2]. Residual strains must be controlled since they can cause misalignments during welding or lead to part geometry out of tolerance. Therefore, most of the time, the parts to be welded are clamped in order to limit strains, concurrently increasing the residual stress level set in the part. Residual stresses are especially problematic in structural assemblies since they will add to the external stresses applied to the part in service, most of the time lowering the in-service lifetime and increasing the risk of failure. For example, the numerical simulation of Ar *et al.* [3] has shown that the higher the clamping force, the lower the strain but the higher the residual stresses in case of 316L stainless steel parts. In addition to the clamping force, the residual stresses are also due to the important thermal gradients developed within the part during the welding operation. Indeed, as explained by Robert [2], during heating, the heated metal is restrained by the cold zones preventing the hot zones from expanding freely. Compressive stresses are then generated, increasing with temperature until the elastic limit of the material is reached. The opposite phenomenon is then observed during cooling. In addition to strain plasticity, solid-state phase transformations can also occur, causing transformation-induced plasticity.

Kou [4] and Robert [2] have proposed several solutions to limit strains during welding. The first one consists in reducing the energy input per length unit to weld the parts, since an extended hot zone of soften metal is the main cause for strains. This can be achieved reducing the length of the weld to reduce temperature gradient extent, by making discontinuous welds, for example. Another way stands in limiting the weld section by chamfering the part to be welded in X instead of V. It enables not only to create opposing strains on both sides of the weld but also to reduce the weld volume and thus the angular strains and the transverse shrinkage. In contrast, a welding process with higher specific energy can also be used to reduce the strains since this enables welds to be made in fewer passes, and therefore reduces the heating time. Finally, the last solution to reduce the residual strain is to pre-deform the part to be welded in the opposite way in order to counteract the strain induced by welding.

A review written by Coules [5] lists some of the techniques used to reduce residual stresses due to welding. The most common method is to apply heat treatments for stress relaxation

afterwards. This method demonstrates successful results on butt weld joints of carbon steels [6] and zirconium alloy [7]. However, it has the disadvantage to increase the strain of the part and is difficult to apply to parts that are too large to be placed in an oven. Moreover, this method is not applicable to all materials since some materials would undergo detrimental microstructural changes, such as phases transformations, during these stress relaxation heat treatments. Localized heating has also been studied and consists of heating the vicinity of the weld bead by an additional heat source (flame, laser, induction) either on the cooled weld or just following the main heat source in order to release the built up stresses. A model developed by Preston *et al.* [8] shows a reduction of the longitudinal residual stress of about 60% in aluminum welded parts. But for the same reasons mentioned above, this method is not applicable to a large number of alloys. Uniform preheating of the base metal can also be carried out on some alloys to reduce residual stresses, decreasing the amount of energy required to melt the metal and lowering the thermal gradient. Still, this method only works on some alloys with particular thermal cycles, such as steels as presented in Asadi's work [9]. In addition, as the yield strength decreases with temperature, this may also introduce additional plastic strain, increasing residual stresses and decreasing the strength of the base metal, as presented in Lin's study on austenitic stainless steel [10]. Localized cooling has also been investigated and consists this time to apply a trailing heat sink (projection of atomized water) at the rear of the heat source. The objective is then to rapidly cool the area that has just solidified and thus increase the temperature gradient, limiting the compressive stresses created during heating. The work of Li *et al.* [11] shows the validity of this technique on TA6V alloy without significant impact onto the mechanical properties of the assembly. Another technique consists to roll the weld or its vicinity, right after welding or during cooling, in order to introduce compressive residual stresses, with the aim to compensate the tensile ones. Altenkirch *et al.* [12] have reached significant results when rolling the weld of aluminum after friction stir welding under a load of 20 kN. Ultrasonic Impact Treatment (UIT) and shot peening can also be used according to the same principle, as Cheng *et al.* did [13] on a A572 Gr.50 steel. They observed better results with the UIT, which has an effect on a larger depth than shot peening. Vibrations can also be applied to the part in order to release stress. However, the effectiveness of this technique is controversial, as is the mechanism that would explain this lowering of residual stress. While Aoki *et al.* [14] have attributed this effect to local strain induced by vibrations in metal already close to its yield point, Walker [15] has rather attributed it to mobile dislocations causing austenite transformation into martensite. Other authors such as Sonsino *et al*. [16] do not measure any effect of vibrations, explaining it by the weight of the welded part (50 kg), latter being close to the application limit given by the distributors of vibration equipment. Eventually, the Global Mechanical Tensioning (GMT) method consist in elastically stretching the assembly in the direction of the weld during welding to create longitudinal stress close to the yield strength and thus allowing stress reduction once released. This method is particularly efficient on thin plates since the effect decreases with the depth of the baseplate, as presented in Altenkirch *et al*. study [17]. However, this method requires expensive equipment and is only applicable to linear welds since the force is applied in the longitudinal direction of the weld.

In summary, all these methods require either pre- or post-processing treatments, or heavy modification of the welding processes. Moreover, in most cases, the studies have only focused

on residual stresses. In contrast, this present work intends to investigate the use of multi-material filler metal to reduce residual strains and stresses simultaneously. Generally, during welding, a unique chemical composition of the filler metal is used. However, several studies have been carried out using an electric arc as heat input, with the deposition of a mix of two different wires. Most of this research focuses on the manufacture of massive parts from alloys produced *in-situ* during the deposition with a mix of two different wires since they cannot be obtained by more conventional manufacturing processes - giving rise to the Double-Wire Arc Additive Manufacturing process (D-WAAM). Uniform materials are thereby obtained, and the authors are thus not focused in residual stresses and strains. For example, Ma *et al*. [18] have developed an *in-situ* titanium aluminum alloy using a TIG torch and two wires, one of pure titanium and the other of pure aluminum. Indeed, titanium aluminum alloys are not available in wire form since they are not ductile enough to be drawn. For the same reasons, it is difficult to machine these alloys, making it appropriate to produce them by additive manufacturing. Actually, Wang *et al*. [19] have demonstrated the possibility to control the phases (α_2-Ti_3Al and γ-TiAl) of titanium aluminum alloys by adjusting the different wires feed speeds and enabling thus to build three walls with three mixtures in different phases proportions. By obtaining a dual microstructure α_2 + γ, a compromise between strength and ductility has been achieved. Cai *et al*. [20] proposed an enhancement by positioning the aluminum wire in the TOP-TIG configuration, i.e. with a small angle between the wire and the torch, while the titanium wire is in the standard configuration, allowing a synchronized melting of the two wires due to their different melting temperatures. Other alloys have also been studied such as aluminum-copper-magnesium alloys by Qi *et al*. [21], using an aluminum-copper wire and a second one of aluminum-magnesium in order to improve the mechanical properties of WAAM aluminum-copper parts by adding magnesium. While there are aluminium-copper-magnesium wires available in the market, they offer limited options for copper and magnesium content. Therefore, double wire processes are attractive as they allow for *in-situ* control of the content of alloying elements. Wang [22] was also interested in the development of nickel-titanium alloys and the impact of process parameters on the microstructure and the mechanical properties. Shen *et al.* [23] manufactured an iron-aluminum intermetallic part by D-WAAM and found its mechanical properties to be better than those of a similar part made by powder fusion process. The same authors also developed a composition graded part by mixing the two wires in different proportions [24]. D-WAAM is also used in other cases, not only for the manufacture of coatings, as Wang *et al.* [25] did when they deposited a nickel-titanium alloy on a titanium part, but also with the plasma process to enhance the deposition rate [26,27]. Most of the authors, in addition to create new alloys or to increase the deposition rate, they are also interested in the mechanical properties of the deposited metal, and thus in the microstructure created : the grain size and morphology, the crystallographic texture, and if there have different phases, their proportions and localizations in addition to the aforementioned characteristics. In particular, Zhang *et al*. [28] have tried to improve the microstructure and strength of a stainless steel by depositing a second filler wire at the back of the molten pool at low speed - its presence disturbing the thermal gradients and hence affecting the solidification and cooling process - with the same composition as the first wire.

Despite recent research on D-WAAM, there are few studies on the effect of using a second filler wire with a chemical composition different from the first one, in particular regarding the establishment of residual strains and stresses. However, one can mention the study of Rodrigues *et al*. [29] where they have determined residual stresses in functionally graded material of 316L stainless steel and Inconel 625 and shown a lower magnitude of residual stresses when the transition between the two materials is rather abrupt, as compared to a graded one.

Among all the materials and alloys studied by D-WAAM, stainless steels remains of a strong interest since they are widely used in many sectors such as energy production, chemical and paper processing, medical and food industries, kitchen equipment manufacturing, transportations, construction and civil engineering. They are mainly used for their anti-corrosive property due to their quite high chromium content and their rather good machinability and formability, making them easily available in many shapes and sizes. Their mechanical and thermal properties vary according to their composition and they are mostly weldable together. Indeed, austenitic stainless steels display higher coefficient of thermal expansion, lower yield stress and lower thermal conductivity than ferritic and martensitic stainless steels, making them more easily deformable during welding [30,31].

This work studies the use of two-filler dissimilar metal on the strains and stresses establishment in the context of deposits produced by the D-WAAM process with a TIG torch onto 304L stainless steel baseplates. This study lays the groundwork for both welding and additive manufacturing applications. To achieve such a purpose, two filler metals, an austenitic 304L and a ferritic 430 stainless steels, are used and mixed in various proportions for the manufacturing of the different studied deposits. The emphasis here is made on a counterbalance of the residual strains and stresses induced regarding the difference in terms of thermal expansion coefficient between the two-filler metals (approximately 17×10^{-6} °C^{-1} versus 10×10^{-6} °C^{-1}, respectively for the 304L and the 430 up to 100°C) [32]. Residual stresses and strains obtained for the different deposits are studied in addition to their microstructure before being discussed together.

2 Experimental procedures

2.1 Materials and Double-Wire Arc Additive Manufacturing set-up

The chemical composition of the 4 mm thick 304L baseplates and of the 1 mm diameter 304L and 430 wires used are presented in Table 1. The main difference lies in their nickel content since the 304L contains 18%wt against 0.35%wt for the 430. Five different single deposits were produced, using either one or two wires (in different proportions) depending on the samples, as summarized in Table 2. Samples have been produced thanks to a D-WAAM process using a TIG system. Schematic representation of the home-made deposition system is introduced in Figure 1. The system is equipped with a single torch and two filler wire dispensers. Movements of the welding torch are controlled thanks to a cartesian robot. The generator used is a TETRIX 301 CLASSIC activArc EWM and the welding torch is an AUT TIG 400 W ABRICOR BINZEL with a ceramic nozzle of 12.5 mm in diameter and a 2% lanthanum tungsten electrode of 2.4 mm in diameter. The shielding gas is pure argon with a flow rate of 12.5 L/min.

	C	Si	Mn	Ni	Cr	P	S	N	Mo	Cu	Co	Fe
Baseplate 304L	0.027	0.34	1.5	8.1	18.2	0.033	0.001	0.051				Bal.
Wire 304L	0.015	0.310	1.550	8.610	18.280	0.035	0.008	0.025				Bal.
Wire 430	0.026	0.43	0.49	0.35	16.98	0.024	0.012	0.0252	0.11	0.12	0.032	Bal.

Table 1: Chemical composition (in weight percent) of the wires and the baseplate according to supplier certificates (PRAUD INOX for the baseplate, WeldFil for the 304L wire and WELD'X for the 430 wire)

Sample name	Baseplate	Wire 1	Wire 2
100% 304L	304L	100% 304L	
25% 430	304L	75% 304L	25% 430
50% 430	304L	50% 304L	50% 430
75% 430	304L	25% 304L	75% 430
100% 430	304L		100% 430

Table 2: Samples produced with different volume proportion of each wire

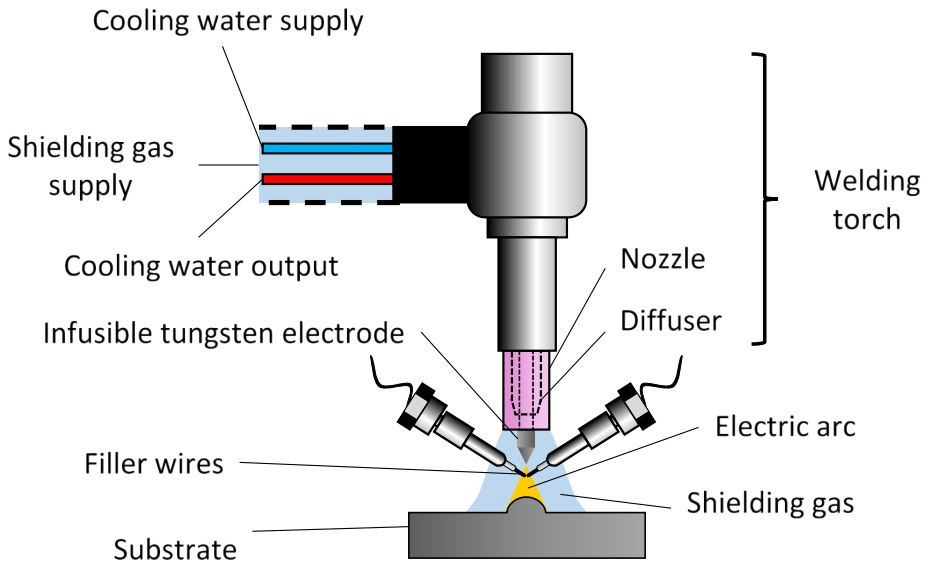

Figure 1: Schematic description of the D-WAAM process with a TIG system

The same process parameters were used for the production of all the parts, i.e. a welding current of 200 A, a welding speed of 15.0 cm/min, a global wire feed speed of 3.7 m/min, an arc height of 4 mm and an angle between the wires and the electrode of 70°. This set of parameters are

suitable for all materials of this study and enable the deposition of both single wires separately without defects. Keeping these parameters equal for each part actually allows to compare residual strains and stresses of all samples independently of the process parameters, i.e. with constant linear energy and material amount input. Indeed, when the two wires are simultaneously deposited, the ratios of those filler metals, and hence the composition of the mix, are controlled adjusting each wire feed speed, while keeping the global filler feed speed (sum of both wire feed speeds) equal to 3.7 m/min for each part. All the parts were produced without clamping the baseplate in order to observe the induced strains and to obtain a better reproducibility of the produced parts. Indeed, Guilmois [33] has observed better reproducibility in the strain measurements of the parts when the baseplate was not clamped as compared to parts clamped with a torque spanner. At least two samples for each composition mix were produced to test the reproducibility.

2.2 Microstructural characterization

Several methods were used to identify the phases set in each deposit, using specimen cut out from each part. Electron Backscatter Diffraction (EBSD) and X-Ray Diffraction (XRD) were used to quantify the fraction of Face-Centered Cubic (FCC) phase (γ austenite) and Body-Centered Cubic (BCC) phases (α ferrite and α' martensite). Since low carbon martensite - which is the type of martensite encountered in this study - and ferrite are both BCC with the same lattice parameter, they are not differentiable using these two technics. Thus, free dilatometry has also been used to identify the mixes that contain martensite in their microstructure.

2.2.1 EBSD cartographies

A fine metallographic preparation is necessary to successfully perform EBSD cartographies. First, samples were cut in the plan perpendicular to the deposit direction. Mechanical polishing was then carried out on grinding paper with silicon carbide from P80 to P4000 followed by a final polishing step with colloidal silica suspension (30 nm particles) on a polishing cloth. Then, sample were electrochemically polished at 5 °C, under 20 V, for 60 s using a LectroPol-5, Struers. The electrolyte composition is 700 mL of ethanol, 200 mL of ethylene glycol monobutyl ether and 100 mL of perchloric acid (70%).

A ZEISS Crossbeam 550L Focused-Ion Beam - Scanning Electron Microscope (FIB - SEM), equipped with an Oxford Instrument Symmetry EBSD camera, was used to acquire the EBSD cartographies. Step sizes between 80 nm and 2.5 µm were used to scan surfaces from 0.014 to 3.4 mm^2 depending of the sample. Samples were tilted at 70° in the SEM chamber and the Aztec software was used to analyze the data sets. Austenite and ferrite/martensite phases were identified using the "Iron bcc (old)" and "Iron fcc" files from the Aztec "HKL phases" database.

2.2.2 X-ray diffraction

For XRD deposit phase analyses, the samples were cut in the plane of the baseplate at the interface between the latter and the deposit along the longitudinal direction of the deposit with a metallographic saw, so that the baseplate was removed and only the deposit remained. The flat cut side of the deposit, which is parallel to the deposition direction, was analysed ensuring no geometrical concerns for phase analysis. Experiments have been performed on a Panalytical

X'Pert Pro diffractometer equipped with a linear Real Time Multiple Strip (RTMS) detector (X'Celerator detector) using Cu K_α radiation (λ = 1.5406 Å). Scans were performed in the 2θ range from 40° to 120° with a scan step of 0.008° and a counting time of 0.08 s per step in Bragg-Bremento mode. Austenite and ferrite/martensite peaks were identified using the JCPDS-card n°00-033-0.97 and 03-065-7752 respectively. The austenite and ferrite/martensite fractions were then evaluated based on their relative integrated intensities as followed, for each identifiable peak pair [34] :

$$V_\gamma = \frac{I_\gamma \times \frac{R_\alpha}{R_\gamma}}{I_\alpha + I_\gamma \times \frac{R_\alpha}{R_\gamma}} \quad (1)$$

$$R = \frac{1}{V^2} \times F^2 \times P \times L \times e^{-2M} \quad (2)$$

$$M = \frac{6h^2T}{mk\Theta^2}\left[\Phi(x) + \frac{x}{4}\right]\left(\frac{\sin\theta}{\lambda}\right)^2 \quad (3)$$

$$x = \frac{\Theta}{T} \quad (4)$$

In equation (1), V_γ is the volume fraction of austenite, I_γ and I_α the integrated intensities of austenite and ferrite/martensite peaks respectively, and R_γ and R_α are computed for each phase using equation (2). In equation (2), V is the unit cell volume, F the structure factor, P the multiplicity factor, L the Lorentz-polarization factor and e^{-2M} the temperature factor where M is calculated using equation (3). To calculate the cell volume, cell parameters of 3.606 Å and 2.877 Å were used respectively for the austenite and the martensite/ferrite. The structure factor F is $4f_\gamma$ and $2f_\alpha$ for respectively the austenite and the martensite/ferrite, f_γ and f_α represent the atomic scattering factor and depends on θ, the position of the considered diffracted peak, and λ, the X-ray wavelength. Equation (3) permits to calculate the temperature factor with h the Planck's constant, m the mass of vibrating atom, k the Boltzmann's constant, and $\Phi(x)$ is a tabulated function that can be found in [34]. In equations (3) and (4), T is the absolute temperature and Θ the Debye characteristic temperature [34]. The values used in this work for the calculations of austenite volume fractions are presented in Table 3 and were calculated with the recommended values given by Cullity [34]. The volume fraction of austenite was determined averaging over 5 to 8 peak pairs. Such calculations assume an isotropic distribution of the cristallographic orientations for both considered phases that will be discussed latter on.

Austenite						Ferrite / martensite					
	2θ (°)	P	L	e^{-2M}	F^2		2θ (°)	P	L	e^{-2M}	F^2
{111}	43.5	8	12.0	0.96	4785	{110}	45.0	12	11.31	0.96	1163
{200}	50.8	6	8.4	0.95	4177	{200}	65.0	6	4.841	0.92	817
{220}	74.8	12	3.6	0.90	2804	{211}	82.3	24	3.127	0.88	632
{311}	90.7	24	2.8	0.87	2275	{220}	98.8	12	2.728	0.85	521
{222}	96.2	8	2.7	0.85	2141	{310}	116.2	24	3.137	0.82	451

Table 3: Values of each constant presented in equations (1) to (4) to calculate the volume fractions of austenite and ferrite/martensite depending on the identifiable peak pairs

2.2.3 Free dilatometry tests

Following XRD measurements, dilatometry tests were performed on samples showing the presence of martensite/ferrite to identify those undergoing an austenitization during heating and a martensitic transformation during cooling. The dilatometer is composed of an oven where the tested sample is heated thanks to halogen lamps and double elliptical mirrors to focus the energy on the sample. A type K thermocouple is welded by spot-welding on the sample and enable to control the sample temperature. The dimensional change of the sample is transmitted through a silica rod to a capacitive sensor, which measures the voltage across the sensor to deduce the elongation or contraction of the sample. Samples were heated up to 950°C at 20°C/min, held at 950°C for 10 min, and then cooled down to room temperature at 20°C/min. As the measured noise is +/- 5 µm, the instrument may detect martensite volume fractions as low as 8%.

2.3 Strain measurements

Macroscopic residual strain of the part has been measured using a laser profilometer composed of a KEYENCE IL-065 laser mounted on the z-axis of a cartesian robot. The spot size is about 550 x 1750 μm^2 at the reference distance of 65 mm. The measurements were achieved in the middle of the part, along the deposition direction at the bottom part surface to measure the baseplate strains only (without confusing with the deposit one's). The resulting scatter plot of the curvature along the length of the baseplate was modelled by a second-degree polynomial curve and the deflection of the part was computed as the difference between the highest and lowest points along the curvature. For the concave plates the deflection is negative whereas for the convex ones the deflection is positive.

2.4 Residual stress determination

2.4.1 Neutron diffraction

2.4.1.1 Principle

Neutron diffraction stress determination is based on the assessment of the distribution of the interreticular distances in space, $d(hkl)$ being used as a strain gauge. The principle of the interreticular distances determination with neutron diffraction relies on Bragg's law:

$$2\langle d(hkl,\varphi,\psi)\rangle_{V_d} sin(\theta_{hkl,\varphi,\psi}) = n\lambda \qquad (5)$$

Where $\langle d(hkl,\varphi,\psi)\rangle_{V_d}$ is the mean value over the diffracting volume, depicted by $\langle\ \rangle_{V_d}$, of the $\{hkl\}$ interplanar distance along the diffraction direction (φ,ψ) of the diffracting grain group. φ and ψ are the azimuthal and tilt angles i.e. the rotational angle around the normal to the sample surface and the angle between the normal to the surface and the normal to the diffracting plane, respectively, as introduced in Figure 2. $\theta_{hkl,\varphi,\psi}$ is the half angle of deflection, i.e. the half angle between incident and diffracted beams in the direction (φ,ψ) for the $\{hkl\}$ plane familly, λ is the wavelength of the beam and n an integer representing the order of reflection.

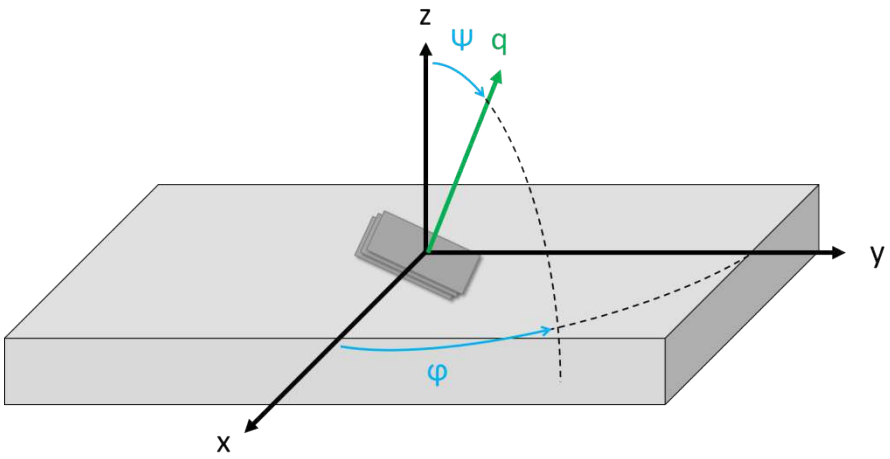

Figure 2: Diagram of axis systems to identify the measurement direction relative to a sample. (x,y,z) corresponds to the part coordinate system and q the direction of measurement.

The strain determination is then given following the rational definition of strain:

$$\langle \varepsilon(hkl,\varphi,\psi)\rangle_{V_d} = ln\frac{\sin\theta_{0_{hkl,\,\varphi,\psi}}}{\sin\theta_{hkl,\,\varphi,\psi}} \qquad (6)$$

Where $\theta_{0_{hkl,\,\varphi,\psi}}$ stands for the peak position of the stress-free material. In the context of morphologically isotropic material without crystallographic texture, the as-followed generalized Hooke's law gives the link between strains and stresses [35]:

$$\begin{aligned}\langle \varepsilon(hkl,\varphi,\psi)\rangle_{V_d} = {} & \frac{1}{2}S_2(hkl)\times\left(\sigma_{xx}\cos^2\phi\ \sin^2\psi + \sigma_{yy}\sin^2\phi\ \sin^2\psi + \sigma_{zz}\cos^2\psi\right)\\ & + \frac{1}{2}S_2(hkl)\times\left(\sigma_{xy}\ \sin 2\phi\ \sin^2\psi + \sigma_{xz}\ \cos\phi\ \sin 2\psi + \sigma_{yz}\sin\phi\ \sin 2\psi\right)\\ & + S_1(hkl)\times(\sigma_{xx}+\sigma_{yy}+\sigma_{zz}) \qquad (7)\end{aligned}$$

Where $\langle \varepsilon(hkl,\varphi,\psi)\rangle_{V_d}$ is the strain measured in the (φ,ψ) direction averaged over the diffracting volume and $S_1(hkl)$ and $\frac{1}{2}S_2(hkl)$ the Radiocrystallographic Elastic Constants (REC).

2.4.1.2 Experimental set-up

Neutron diffraction measurements were performed on the SALSA beamline from the Institut Laue Langevin in Grenoble, France [36]. SALSA is an instrument dedicated to the measurement of lattice strains of many materials, thanks to a hexapod enabling both translations and rotations.

Lattice strains were measured along the three main directions x, y and z of the part coordinate system in order to get cartographies of residual stresses along the three orthogonal directions (longitudinal, transverse and normal to the deposition direction). Measurements were performed in a plane perpendicular to the deposition course, in the middle of the part i.e. in the

stationary regime, in both baseplates and deposit, as presented in Figure 3 with the black and white cubes. Measurements were achieved on only one side of each part, due to the symmetry of the samples, with irradiated volumes becoming increasingly spaced as they move away from the melted zone. In order to ensure reliable stress-free measurements, for each part, a twin sample was produced in the exact same conditions. One has been used to determine the stresses, and the second one has been used to extract volume gauge volumes (2.8 x 2.8 x 2.8 mm^3 cubes) in the exact same locations where the neutron measurements have been achieved within the first part. Each θ_0 was measured along the same three orthogonal directions on the cubes of the five investigated samples, dug out using electro-erosion cutting enabling accurate position extraction, without work-hardening (nor associated microstructure changes) and a stress relief. θ_0 measurements were performed for each gauge position of the 100% 304L sample, and for each measurement point where a microstructure change is expected for the other samples, corresponding to the green cubes in Figure 3.

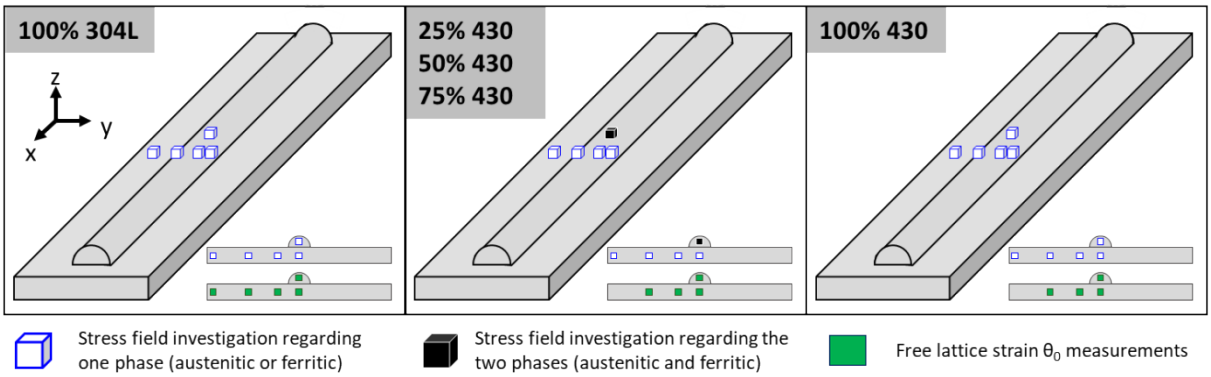

Figure 3: Diagram of the different samples and localizations of the measurement points.

Based on the studied stainless steel nature and on EBSD measurements performed on similar samples beforehand, two different gauge volumes of 0.6 × 0.6 × 2 mm^3 and 2 × 2 × 4 mm^3 have been used, compromising between acceptable counting time, suitable as regard to the expected stress gradient magnitude, and the sample microstructure (mainly grains size consideration). The gauge volume of 0.6 × 0.6 × 2 mm^3 was used for the free lattice strain measurements, and for the longitudinal direction of each sample. The gauge volume of 2 × 2 × 4 mm^3 was used for the two last directions in order to get improved signal-to-noise statistics. One can notice that this gauge volume could not be used for the longitudinal direction due to the size of the deposits which are not high enough.

The wavelength has been set at 1.64878 Å so that Bragg reflections of interest, $\{311\}_{FCC}$ (austenite) and $\{211\}_{BCC}$ (ferrite), are brought to scattering angles of about $2\theta = 101°$ and 91° respectively. Indeed, in order to determine the stresses as accurately as possible, it is necessary to make peak measurements at relatively large diffraction angles, in order to measure a significant angle shift. The diffraction angles analyzed are therefore close to 90°, since these are the ones that show the most accurate peak positioning [37,38].

Diffraction patterns have been analyzed thanks to LAMP (Large Array Manipulation Program) software using a pseudo-Voigt curve-fitting algorithm. Longitudinal (σ_{xx}), transverse (σ_{yy}) and normal (σ_{zz}) residual stresses were computed as follows [39]:

$$\begin{cases} \sigma_{xx} = \frac{1}{\frac{1}{2}S_2(hkl)}\left(\varepsilon_{xx} - \frac{S_1(hkl)}{\frac{1}{2}S_2(hkl) + 3S_1(hkl)}(\varepsilon_{xx} + \varepsilon_{yy} + \varepsilon_{zz})\right) \\ \sigma_{yy} = \frac{1}{\frac{1}{2}S_2(hkl)}\left(\varepsilon_{yy} - \frac{S_1(hkl)}{\frac{1}{2}S_2(hkl) + 3S_1(hkl)}(\varepsilon_{xx} + \varepsilon_{yy} + \varepsilon_{zz})\right) \\ \sigma_{zz} = \frac{1}{\frac{1}{2}S_2(hkl)}\left(\varepsilon_{zz} - \frac{S_1(hkl)}{\frac{1}{2}S_2(hkl) + 3S_1(hkl)}(\varepsilon_{xx} + \varepsilon_{yy} + \varepsilon_{zz})\right) \end{cases} \quad (8)$$

The REC used for residual stresses calculation are presented in Table 4. The assumptions made here are that the grain shape is spherical and the texture isotropic. In areas where there is both austenite and ferrite/martensite, phases volume fractions were identified beforehand, allowing the calculation of residual stress by a mixing law after measuring the strains for each phase, as suggested by Hauk [35].

	$\{311\}_{FCC}$	**$\{211\}_{BCC}$**
$S_{1\{hkl\}}$ (x10^{-6} MPa^{-1})	-1.6084	-1.2072
$\frac{1}{2}S_{2\{hkl\}}$ (x10^{-6} MPa^{-1})	7.0314	5.5864

Table 4: REC of austenite and ferrite/martensite used for residual stresses determination

Error bars corresponds to the statistical uncertainty associated with the integration over the detector height, where $\delta\theta$ is the peak position uncertainty given by LAMP software for each fit [39]:

$$\begin{cases} \delta\varepsilon_{xx} = \sqrt{\left(\frac{\delta\theta_{0_{hkl,\,0,90}} \times \cos\theta_{0_{hkl,\,0,90}}}{\sin\theta_{hkl,\,0,90}}\right)^2 + \left(\frac{\delta\theta_{hkl,\,0,90} \times \cos\theta_{hkl,\,0,90} \times \sin\theta_{0_{hkl,\,0,90}}}{\sin^2\theta_{hkl,\,0,90}}\right)^2} \\ \delta\varepsilon_{yy} = \sqrt{\left(\frac{\delta\theta_{0_{hkl,\,90,90}} \times \cos\theta_{0_{hkl,90,90}}}{\sin\theta_{hkl,\,90,90}}\right)^2 + \left(\frac{\delta\theta_{hkl,\,90,90} \times \cos\theta_{hkl,\,90,90} \times \sin\theta_{0_{hkl,\,90,90}}}{\sin^2\theta_{hkl,90,90}}\right)^2} \\ \delta\varepsilon_{zz} = \sqrt{\left(\frac{\delta\theta_{0_{hkl,\,0,0}} \times \cos\theta_{0_{hkl,\,0,0}}}{\sin\theta_{hkl,\,0,0}}\right)^2 + \left(\frac{\delta\theta_{hkl,\,0,0} \times \cos\theta_{hkl,\,0,0} \times \sin\theta_{0_{hkl,\,0,0}}}{\sin^2\theta_{hkl,\,0,0}}\right)^2} \end{cases} \quad (9)$$

$$\begin{cases} \delta\sigma_{xx} = \frac{2}{S_2(hkl) \times (S_2(hkl) + 6S_1(hkl))} \times \sqrt{((S_2(hkl) + 4S_1(hkl)) \times \delta\varepsilon_{xx})^2 + 4S_1(hkl)^2 \times (\delta\varepsilon_{yy}{}^2 + \delta\varepsilon_{zz}{}^2)} \\ \delta\sigma_{yy} = \frac{2}{S_2(hkl) \times (S_2(hkl) + 6S_1(hkl))} \times \sqrt{((S_2(hkl) + 4S_1(hkl)) \times \delta\varepsilon_{xx})^2 + 4S_1(hkl)^2 \times (\delta\varepsilon_{xx}{}^2 + \delta\varepsilon_{zz}{}^2)} \\ \delta\sigma_{zz} = \frac{2}{S_2(hkl) \times (S_2(hkl) + 6S_1(hkl))} \times \sqrt{((S_2(hkl) + 4S_1(hkl)) \times \delta\varepsilon_{xx})^2 + 4S_1(hkl)^2 \times (\delta\varepsilon_{xx}{}^2 + \delta\varepsilon_{yy}{}^2)} \end{cases} \quad (10)$$

2.4.2 Contour method

The contour method is a destructive method allowing the residual stress field determination in one direction for a section of a part. This method consists in cutting the part along the measurement plan, in order to relax the stress, usually by Electrical Discharge Machining (EDM) - present case. Latter enables to obtain a straight cut, without removing excess material or adding residual stress. The material strain due to stress relaxation is then measured by profilometry on one of the two halves of the sample. Then, a 2D Finite Element (FE) method is used with the displacement measured in the previous step by profilometry as input data. An external force required to cancel the strain is virtually applied to the surface, and the resulting simulated stress field is representative of the one that was initially present in the part before cutting it. The contour method was performed on the 100% 304L sample. In order to compare these results with those obtained by neutron diffraction, the cartography of the longitudinal residual stress was performed in the same measurement plane. Two sacrificial pieces made of 304L material and perfectly fitting the shape of the final part are set above and below it in order to ensure a constant section to be cut by EDM. This permits to keep the EDM cutting parameters constant and reduces cutting artefacts. Once clamped, the sample was cut in the median transverse plane by EDM with a Fanuc Robocut A-C600iB and a brass wire of 150 µm diameter. The strain of the material was then measured with an Alicona InfiniteFocus. To calculate the displacement profile, a data correction has been applied to align the displacement of the two opposing faces. To remove measurement artefacts and reduce possible excessive roughness, a filter is applied. Data are then interpolated by a 2D numerical spline function, which is then discretized for modelling. Then, the discretized data from both sides are averaged to remove errors due to the shear stress and antisymmetric displacement errors of the EDM. Stresses have been calculated by FE modelling with Gmsh 4.4.1 software and Aster code considering a material with an isotropic elastic behaviour. Elastic constants E = 200 GPa et ν = 0.33 were used and results were averaged over successive 2 x 2 mm² surface areas, matching the surface of the gauge volume taken in neutron diffraction experiments to make the comparison with the contour method easier.

3 Results

3.1 Phases identification

3.1.1 EBSD

Figure 4 presents the fractions of identified phases by EBSD as well as fraction non-indexed in the 5 investigated deposits. Samples display FCC phase (γ austenite) and/or BCC phases (α ferrite and α' martensite). One can note that ferrite and martensite are not differentiable either by EBSD or by XRD since they have the same crystallographic structure, due to the low amount of carbon in the studied stainless steels. EBSD cartographies show a majority of austenite in the 100% 304L

and a majority of ferrite and/or martensite in the mixes with 50% or more of 430. In the 25% 430 sample, a mix of the two structures is indexed. However, depending on the samples, between 4% and 27% of analysed surface are not indexed. Overall, the more there is 430 in the mix, the less there is austenite and the more there is ferrite/martensite.

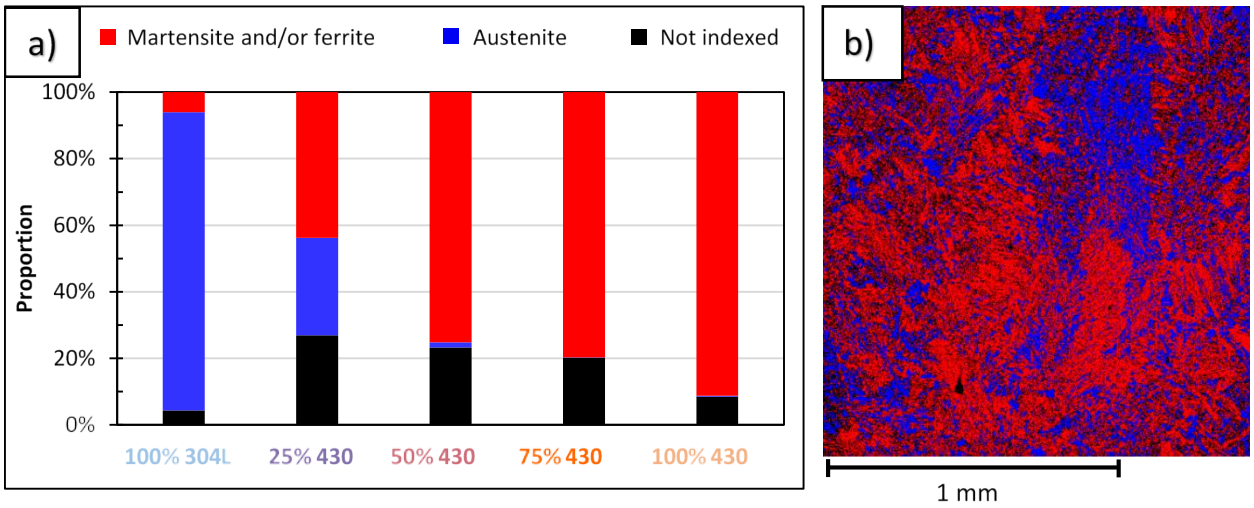

Figure 4: (a) Fractions of austenite, martensite/ferrite and unindexed area in each sample evaluated by EBSD analysis, (b) an example of an EBSD cartography obtained on the 25% 430 sample showing austenite in blue and ferrite/martensite in red

3.1.2 XRD

Figure 5 introduces the different diffraction patterns obtained for the 5 samples. The expected position of the diffraction peaks of each phase is shown by vertical lines in blue for austenite and in red for ferrite/martensite. XRD analyses show the presence of austenite peaks in 100% 304L and in 25% 430 samples, as expected considering the EBSD results, but also in the 50% 430 sample, where no austenite was found, according to previous EBSD cartographies (Figure 4). The peaks of the BCC phases are indexed in all specimens with different intensities depending on the samples. Figure 6 shows the average value of austenite fraction evaluated with the integrated intensities method for each sample. One observes here also that the more there is 430 in the mix, the less there is austenite within the deposit.

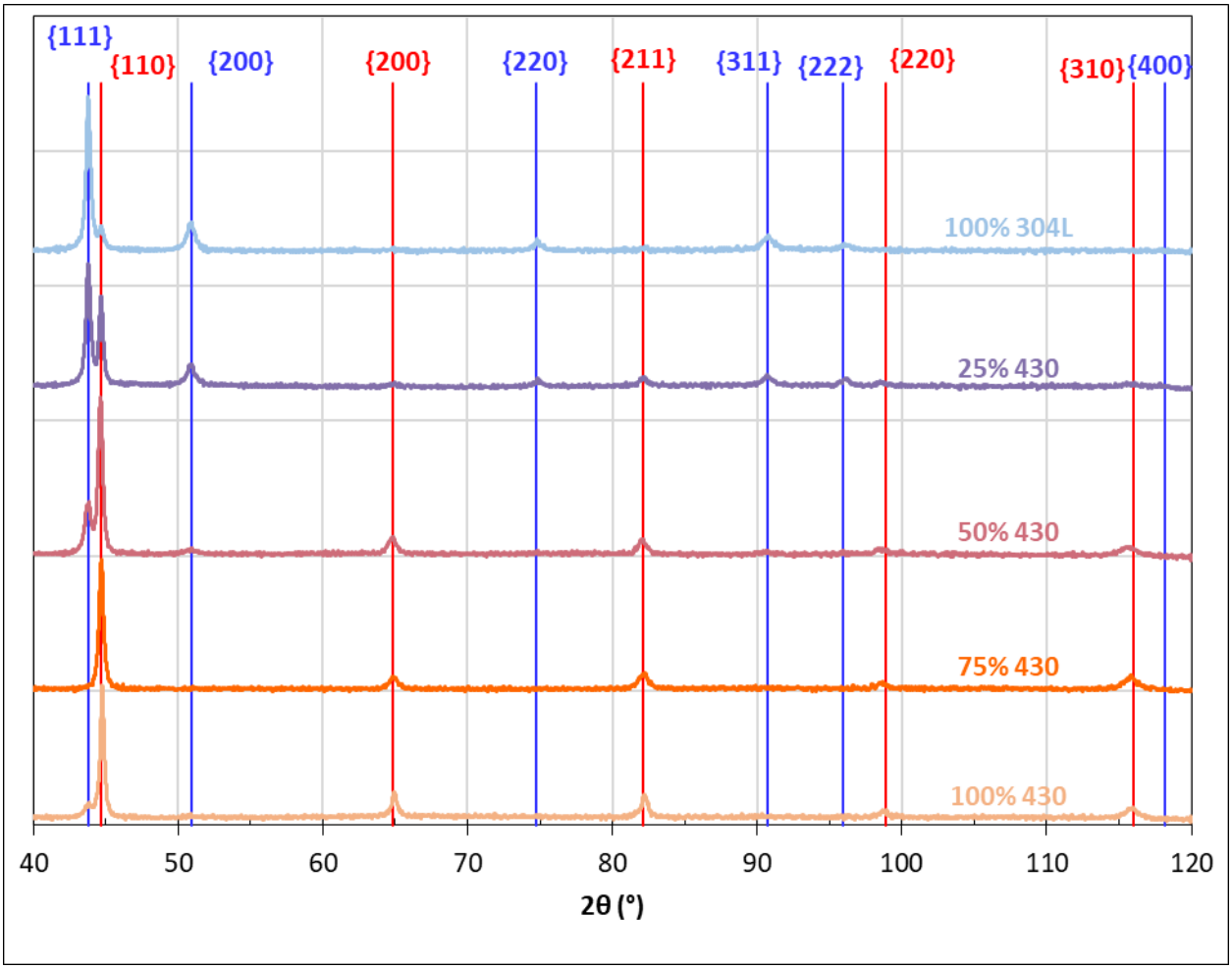

Figure 5: X-ray diffractograms obtained after measurement on the back side of the cut deposit for the 5 samples. Blue and red vertical lines give expected peaks positions for respectively the austenite and bcc phases (ferrite and martensite)

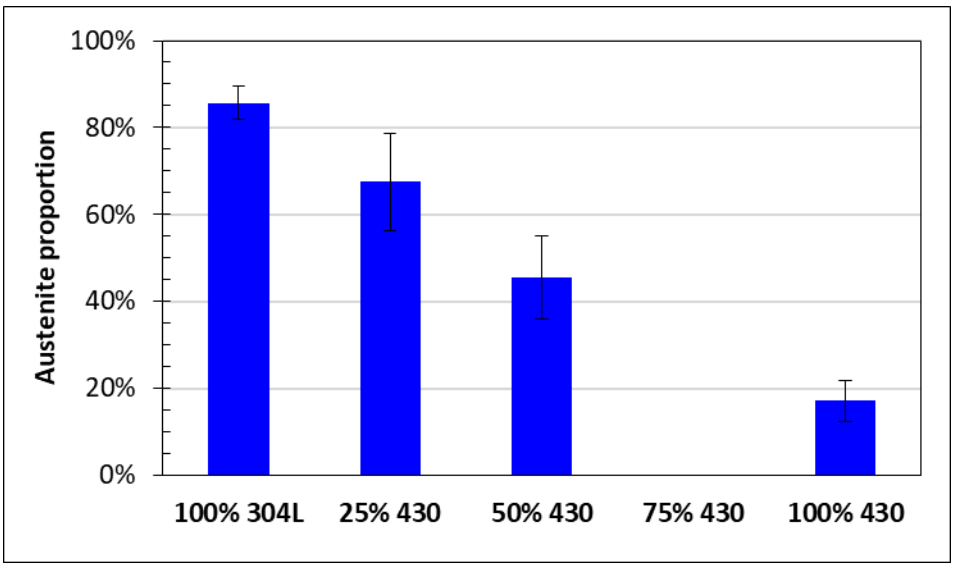

Figure 6: Fraction of austenite evaluated by X-Ray diffraction with the integrated intensities method in each deposit cut out from the 5 investigated samples.

3.1.3 Free dilatometry

Figure 7 displays the dilatometry curves, i.e. the strain as a function of temperature, for the 5 investigated samples. They show the austenite transformation during heating for the samples with 50% or more of 430. In the same way, a phase transformation upon cooling is observed very slightly for the 50% 430 sample and very strongly for samples with 75% or more of 430, indicating the presence of martensite at ambient temperature within these deposits. One can note that the martensite start (Ms) seems to increase with the amount of 430 in the mix, as well as the intensity of the transformation, which could indicate that the more 430 in the mix, the more martensite there is.

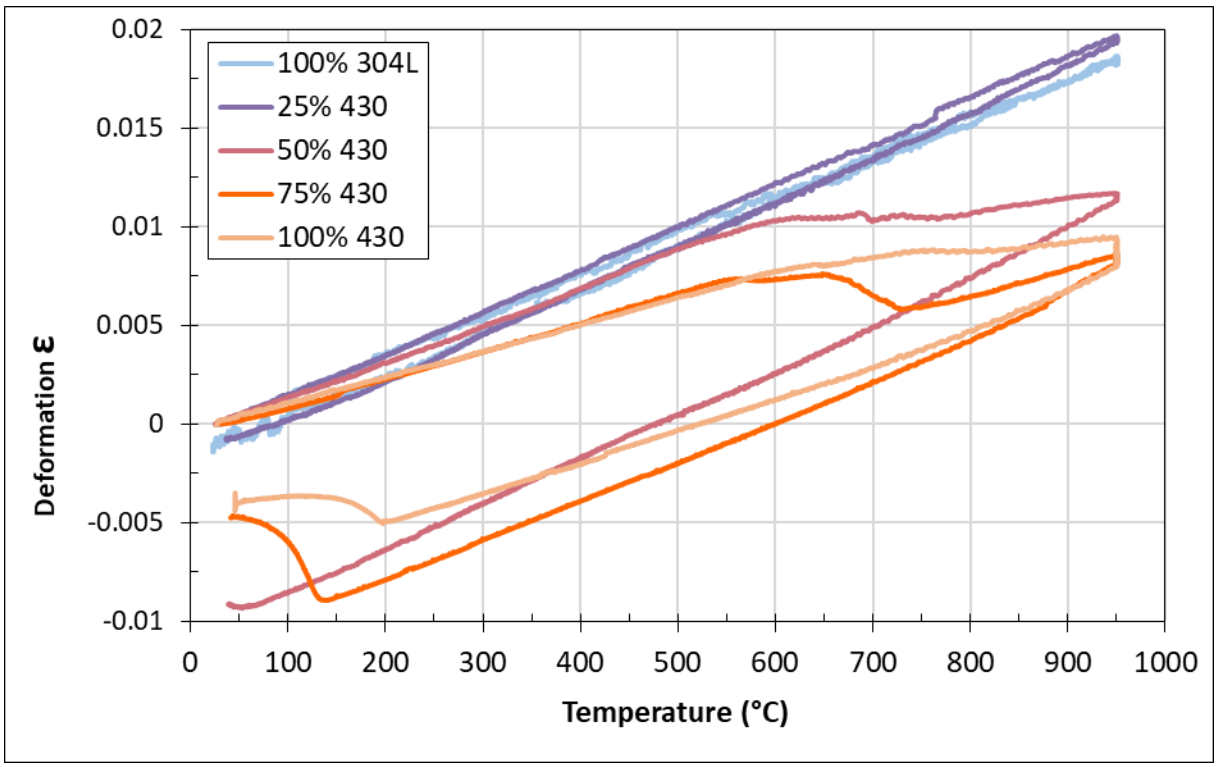

Figure 7: Dilatometry curves showing strain as a function of temperature during free dilatometry tests conducted on samples cut out from each deposit

3.2 Residual strains

Figure 8 presents the deflections measured by profilometry after cooling on each sample along the deposition direction. Results show that the more ferritic 430 in the mix, the lower the deflection. 75% 430 samples are interesting since they show quasi-zero deflections on average, some of them being slightly reversed to a concave plate.

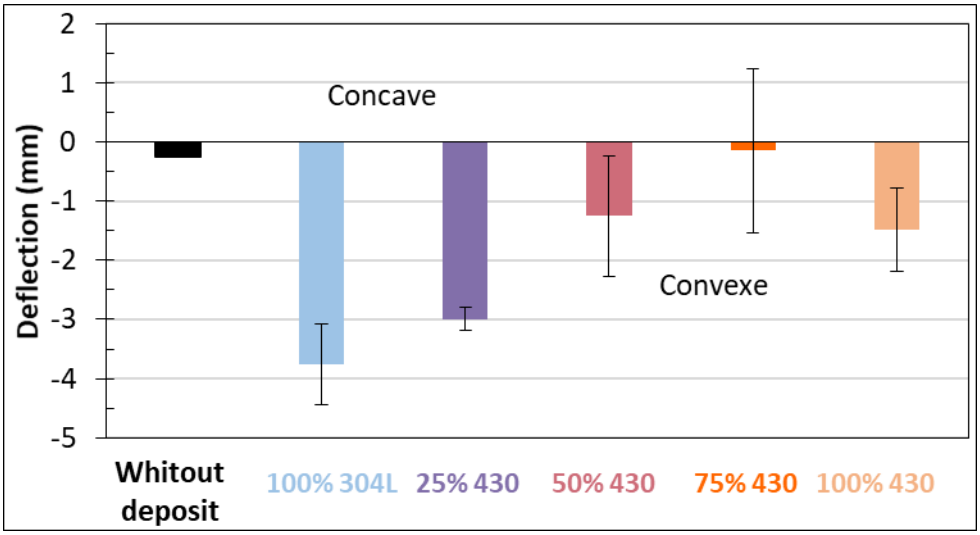

Figure 8: Deflection obtained for each sample after cooling. Error bars correspond to minimum and maximum deflection.

3.3 Residual stress

3.3.1 Neutron diffraction

Figure 9 a) shows the longitudinal, transverse and normal residual stresses determined by neutron diffraction, in the baseplate of the 100% 304L sample at the measurement points shown in Figure 3. Results show that the longitudinal residual stress is more important than the transverse and normal ones, which are both of the same magnitudes. In addition, tensile residual stresses were obtained close to the deposit and compressive ones near the edges. The same trend was observed for the other samples.

Figure 9 c) presents the longitudinal residual stress in the baseplate of each sample, showing that when two wires are used simultaneously, the longitudinal stress is reduced close to the deposit. However, far from the deposit, the residual stress is more important or equal to those of the 100% 304L sample. The 50% 430 sample is interesting since its longitudinal stress is reduced by about 40% close to the deposit and is similar to the one of 100% 304L far from the deposit.

Figure 9 b) shows the longitudinal residual stresses obtained in the deposits. Results show tensile stresses in the austenitic deposit (100% 304L) but compressive or close to zero residual stresses in the ferritic/martensitic deposits (100% 430 and 75% 430) and in the biphasic ones (austenite and ferrite/martensite for 50% 430 and 25% 430). One can note that in the 25% 430, the austenitic phase is under tensile residual stress while the BCC phase(s) is (are) rather in compression.

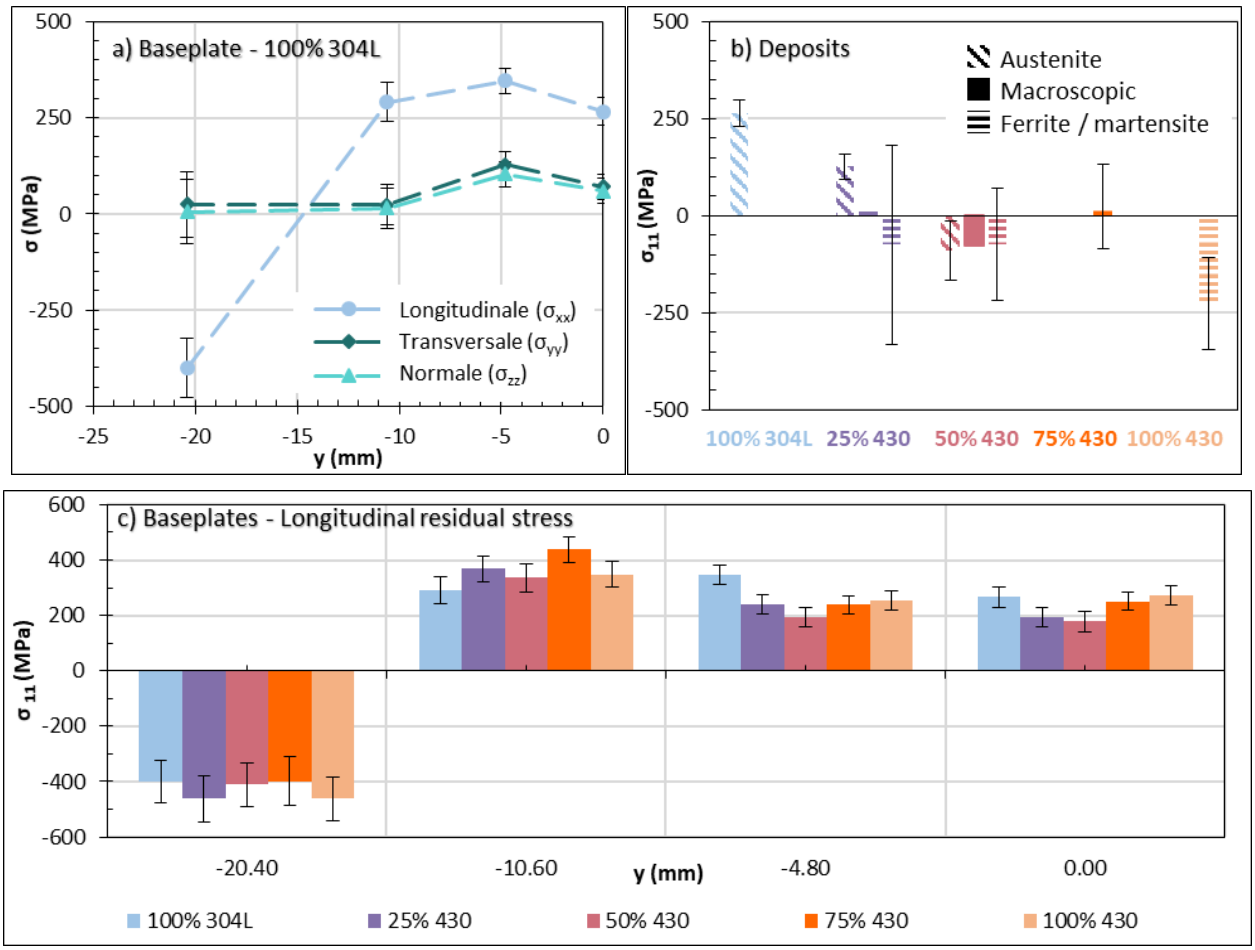

Figure 9: Residual stresses obtained with neutron diffraction (y = 0 corresponds to the middle of the plate's width). a) Longitudinal, transverse, and normal residual stresses in the baseplate of the 100% 304L sample measured across the width. b) Longitudinal residual stresses measured in the deposit of each sample for austenite or ferrite/martensite. When the deposit is biphasic, the macroscopic stress is calculated according to a mixing law. c) Longitudinal residual stresses measured in the baseplate across the sample width for each sample.

3.3.2 Contour method

Figure 10 presents the longitudinal residual stress profile in the middle of the 100% 304L part obtained with the contour method. Tensile residual stress is observed in the deposit and close to the deposit with a maximum reached in the bottom region of the baseplate set between 800 and 1000 MPa. Compressive residual stress is obtained near the baseplate edges with a maximum in absolute value reached in the upper region of the baseplate and set between -800 and -1000 MPa. In most of the section, residual stresses lies between -600 to 600 MPa.

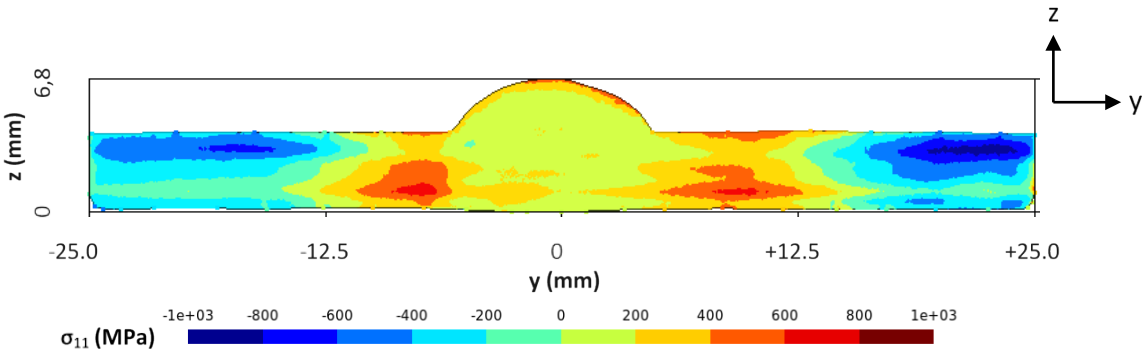

Figure 10: Longitudinal residual stress mapping obtained with the contour method, in the middle of the 100% 304L sample, along the transverse direction

4 Discussion

4.1 Identification of the phases in the deposits

Considering only EBSD cartographies (Figure 4), the fraction of each phase is not precisely known since a significant portion of the surface (around 25%) is not indexed, especially for the 25%, 50% and 75% 430 samples. Non-indexed areas could correspond to either grain boundaries, a too fine microstructure, or a plasticity effect, leaving a doubt regarding the nature of the phases set in the non-indexed areas. Furthermore, areas which were initially austenitic could have been transformed in martensite due to the surface preparation protocol (during the mechanical or electrochemical polishing step). Indeed, Baghdadchi *et al.* [40] have observed that mechanical polishing can introduce strain-induced martensite in duplex stainless steels. Performed XRD phase investigation based on integrated intensity analyses can give an estimate of the phase volume fractions (Figure 6). This method meet also some limitations since present analysis does not take into account the texture effect. Indeed, the crystallographic texture of the alloy can modify the intensity of the peaks, and thus the calculation of the phase proportion. However, EBSD cartographies have shown a maximal MUD (Multiples of Uniform Distribution) set between 2.4 and 5.7 depending on the sample, suggesting that the phase proportions determined from XRD averaging over numerous peak pairs should still representative of the actual ones. Furthermore, the low dispersion of the results supports the fact that our samples have few crystallographic textures and the validity of this analysis. Figure 11 shows a comparison of the results obtained by the two methods (EBSD and DRX). For the 25% and 50% 430 deposits, the comparison of the two methods shows that at least a great part of the non-indexed areas in EBSD could corresponds to austenite in these samples. Also, it is possible that some areas are preferentially indexed as ferrite/martensite while there is also austenite, but in the form of grains smaller than the size of the interaction volume of the backscatter electrons. In order to confirm this hypothesis, TEM analyses were carried out in the 50% 430 sample, using Automated Crystal Orientation Mapping for Transmission Electron Microscopy (ACOM-TEM) [41], using the Nant'Themis, a TEM Themis Z G3 Cs-probe corrected microscope (Thermo Fisher Scientific) [42]. A 17 nm needle of austenite was observed (Figure 12) which could be close to the size of

the interaction volume of the backscatter electrons. Combining the two technics (EBSD and DRX) allows us to obtain a relevant average estimate of the austenite volume fraction in each sample. Moreover, free dilatometry tests (Figure 7) allowed the identification of samples displaying martensite. It is observed, that the 50% 430 sample has a very low amount of martensite since the martensite transformation is hardly visible. However, the latter is largely present for the 75% and 100% 430 samples. Thanks to these three methods of microstructural characterisation, a range of austenitic and ferritic/martensitic fractions is therefore proposed for each sample in Table 5.

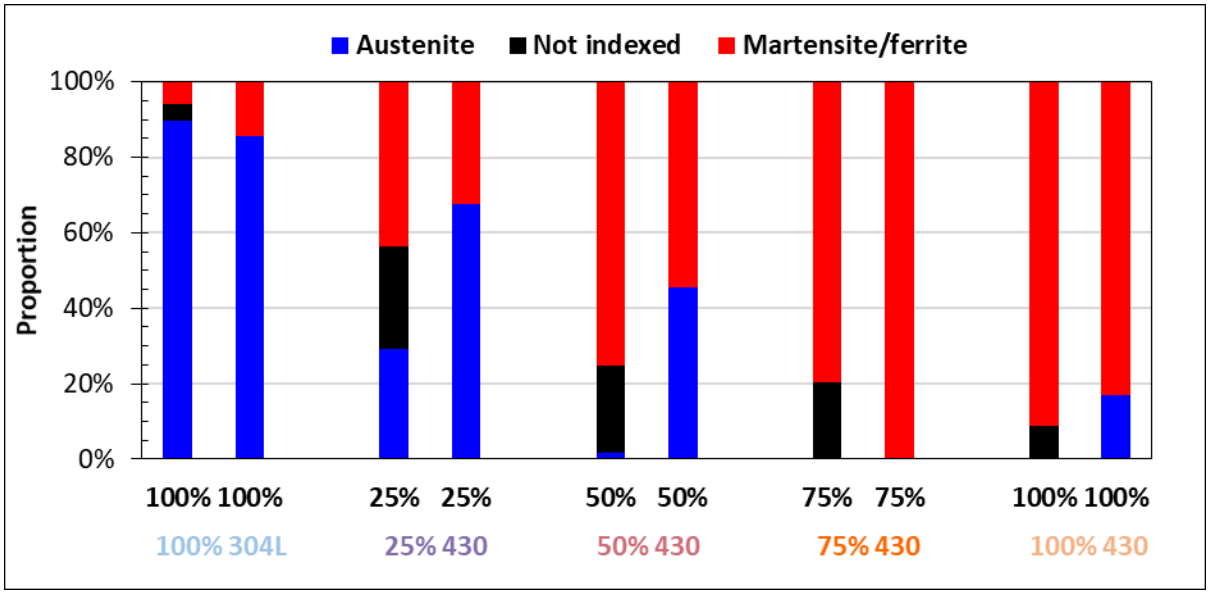

Figure 11: Comparison of the evaluation of the fractions of austenite and ferrite/martensite by EBSD, and by XRD with the integrated intensities method

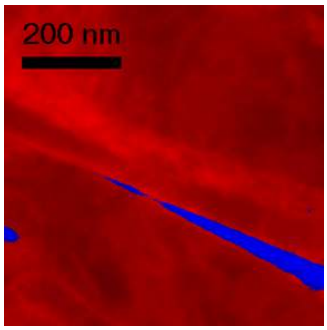

Figure 12: ACOM-TEM mapping on 50% 430 sample showing phase distribution. Red and blue areas correspond respectively to BCC and FCC phases

100% 304L	=	90 – 94% austenite	+	6 – 10% ferrite
25% 430	=	29 – 56% austenite	+	44 – 71% ferrite
50% 430	=	2 – 25% austenite	+	75 – 98% martensite/ferrite
75% 430	=			100% martensite/ferrite
100% 430	=	0 – 9% austenite	+	91 – 100% martensite/ferrite

Table 5: Volume fraction estimates of austenite and ferrite/martensite in each deposit based on the confrontation of EBSD, XRD and dilatometry results

Highly resolved Energy Dispersion X-Ray mapping (EDX) can identify depleted and enriched areas of either nickel or chromium, as did Yu P. *et al*. Areas enriched in chromium and nickel corresponding respectively to ferrite and martensite, since ferrite is inherited from solidification and martensite is stemming from austenite transformation upon cooling [43]. However, here again, the size of the volume analysed by the EDX probe is probably too large compared to the size of the microstructure features, making it impossible to differentiate them.

The average composition of each deposit measured by EDX was positioned on a Schaeffler diagram [44]. As shown in Figure 13, all three mixtures are in the three-phase (A + M + F) region. No martensite was identified in the 25% 430 sample with dilatometry curve, and no austenite was found in 75% 430 either by EBSD or by XRD. However, as they are close to respectively the A + F and the M + F boundaries, it may have few martensite/austenite unidentifiable with these methods of characterization. Moreover, some elements, such as cobalt and nitrogen, are not taken into consideration in the calculus of chromium and nickel equivalent and can affect their positioning on the Schaeffler diagram, since those are gamma promoting elements. In addition, the cooling rate may be different from that in which the diagram was calculated, shifting the domain boundaries. Overall, our conclusions are consistent with the Schaeffler diagram as all three phases were identified in our samples, and the more there is 430 in the mixture, the less there is austenite and the more there is ferrite.

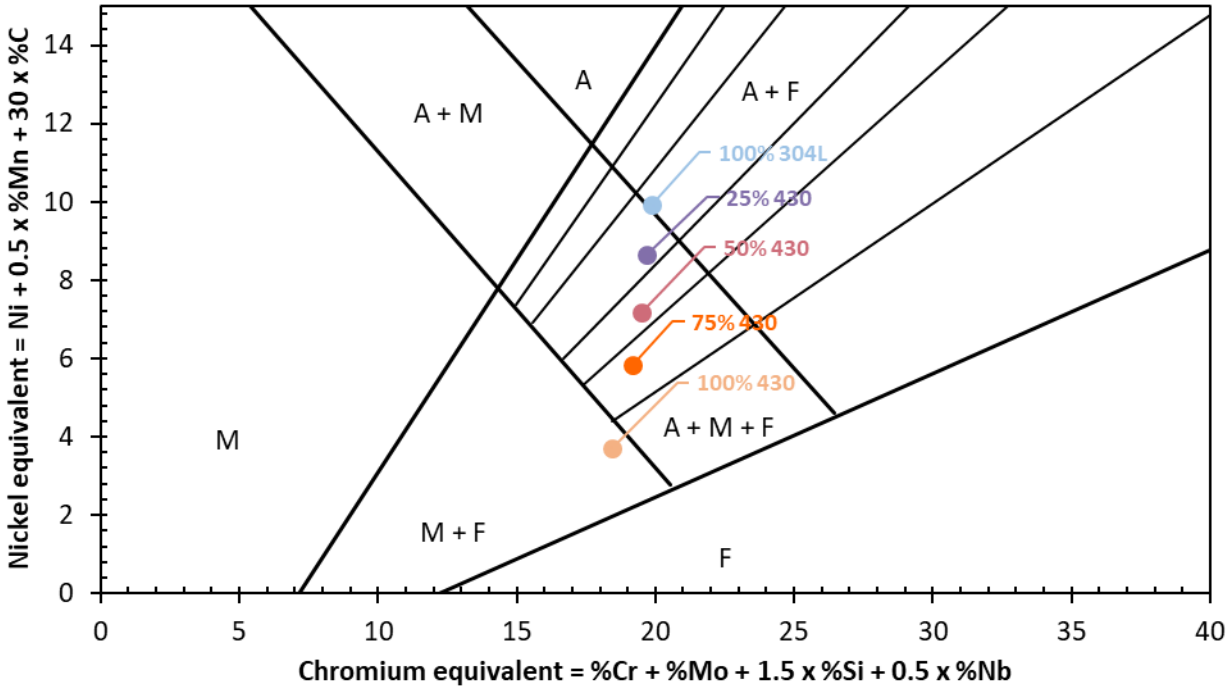

Figure 13: Positioning of the composition of each deposit on the Schaeffler diagram thanks to EDX measurement

4.2 Comparison of two methods for determining residual stresses

Neutron diffraction (Figure 9) and the contour method (Figure 10) have been used to determine residual stresses in the 100% 304L sample. The compared results show good agreement, with a difference of less than 100 MPa (Figure 14). The observed difference could be attributed to the fact that in neutron diffraction stress analysis, the assumptions of isotropic texture with equiaxed grains are made. These assumptions about the microstructure are not completely verified, neither in the baseplate, which was rolled, nor in the deposit, which has large columnar grains oriented along the cooling gradient. Despite all, these assumptions seem to be allowable in this case to give a good estimation of the residual stresses within the part. Indeed, as previously mentioned, the maximum MUD is relatively low (3.6 for 100% 304L), and the grain size shape factor is not very pronounced (size ratio of 2.2, 2.3, 1). Concerning the contour method, as explained by Hosseinzadeh *et al.* [45], measurement errors may occur if the cut does not follow a perfectly defined surface, if material is removed during the cut, if the method introduces additional stresses, and if it plastically deforms the part. However, all precautions have been taken to limit these effects. Overall, a good correspondence of results was obtained between neutron diffraction and the contour method with differences ranging from 5 to 100 MPa depending on the measurement areas. Jacob *et al.* 2018 also compared the two methods in a thick steel weld where results show good correspondence with a maximum difference of 50 MPa [46].

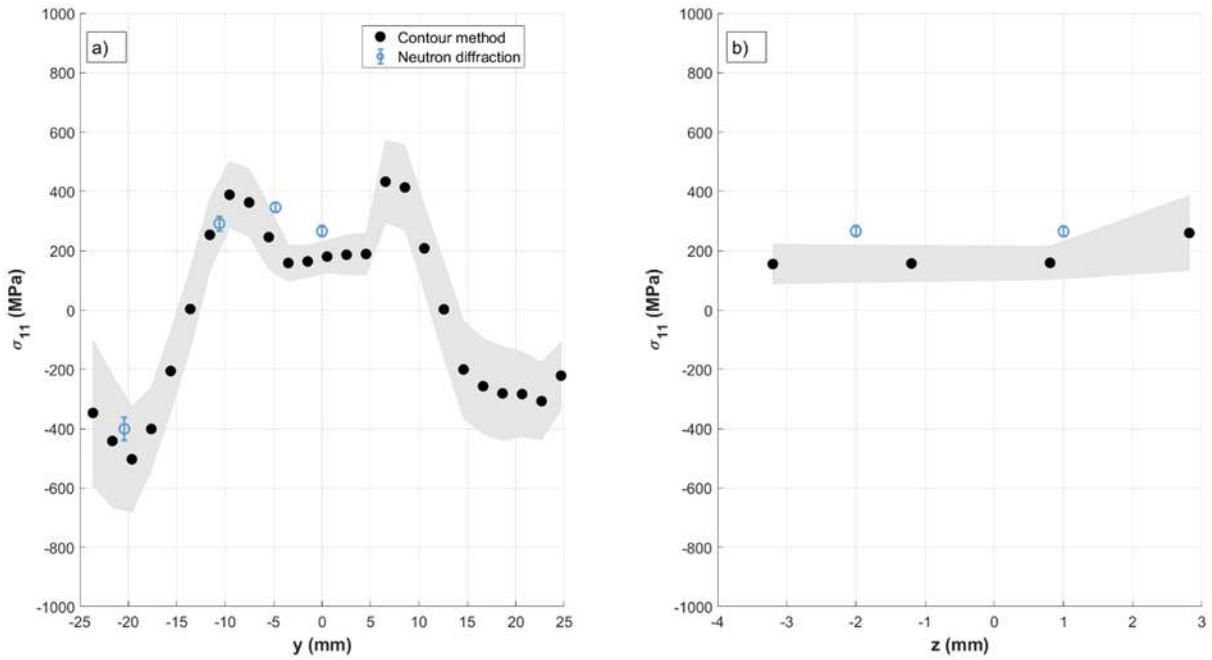

Figure 14: Comparison of neutron diffraction and contour method on the longitudinal residual stress along a) y-axis and b) z-axis. Grey surface corresponds to the combined standard uncertainty taking into account the dispersion of the results over the surface on which the average stress was calculated, and the uncertainty related to the contour method, estimated at 50 MPa

4.3 Link between microstructure, strain, and residual stresses

Comparing the residual stress results (Figure 9) with those of the phase volume fractions (Table 5), one can observe that compressive or close to zero stresses are obtained in deposits containing martensite. Indeed, during a martensitic transformation, the FCC austenite changes to a less compact BCC lattice structure. The expansion of the structure upon transformation thus leads to the establishment of compressive residual stresses within the formed phase (martensite). As Katemi [47] observed, the larger the martensite fraction, the higher the compressive stresses. The lower the temperature at which the martensitic transformation takes place, the less additional tensile stresses will establish upon the rest of the cooling process, and thus the more these zones can be maintained in compression. Indeed, if the martensitic transformation occurred at higher temperature, after the transformation, the part still contracts during the rest of the cooling, inducing additional tensile stress that will, at best, lower the compressive stress established upon transformation and, in the worst case, bring back a tensile state in the cooling zones [48]. However, according to our results (Figure 9), a too high martensite fraction seems to increase the magnitude of tensile stresses in the baseplate to compensate for the compressive stresses in the bead. We have observed that the sudden bead expansion, induced by the martensitic transformation upon cooling, reverses the displacement direction of the baseplate (Figure 8). Indeed, just after deposition, the baseplate of the 75% 430 sample is deformed concavely but then this strain regressed during martensitic transformation, sometimes becoming

even convex depending of the sample, several minutes after the end of the deposition, when the temperature of Ms is reached.

Regarding presented results, depositing a three-phase bead, with some martensite, ferrite and austenite, would allow a compromise between strain and stress. Ferrite, having a lower coefficient of thermal expansion than austenite, would allow the baseplate to deform less than a fully austenitic bead. The martensitic transformation would cause the domed sheet phenomenon, thus reducing the final strain. Lower stresses would then be introduced into the part, as in the case of the 50% 430 part.

Indeed, this mixture is particularly interesting since it allows reducing the stresses near the bead, while keeping them at a reasonable level away from the bead, as compared to parts built with a single wire. Furthermore, in the bead, stresses are close to zero, or even in compression, which is interesting in order to improve the fatigue life of the parts in service [48]. Moreover, at the same time, the 50% 430 part had reduced strains by an average of 67% as compared to the 100% 304L part.

5 Conclusions

The D-WAAM process with a TIG system enables to depose a mixture of austenitic 304L and ferritic 430 stainless steel wires onto a 304L baseplate. The present work compares the residual stresses and strains, and microstructures of the resulting parts.

- This study showed the complexity of identifying the austenite proportion in stainless steel deposits with EBSD, since a significant area of the samples could be non-indexed, despite a careful metallographic preparation.
- If the measured area has little crystallographic and morphological texture, XRD can correctly quantify the proportion of austenite, using the relative integrated intensities of a maximum number of identifiable peak pairs.
- Free dilatometry test makes it possible to identify samples with martensite.
- Mixing two filler wires with different chemical compositions and thermal expansion helped to reduce strains and stresses. Indeed, with the mixt 50% 430, a three-phase microstructure (austenite, ferrite and martensite) reduced strains by 67% and residual stresses were either reduced by 40%, in both the deposit and the base metal, or at least maintained, depending on the analyzed area.
- A good correlation of the results was obtained with the contour method and neutron diffraction with a good match (differences of less than 100 MPa).

To conclude, using two filler wires presenting differences in thermal properties could present a good interest in reducing residual stresses and strains, in the context of both additive manufacturing and welding. Future studies will be carried out to determine the residual stresses and strains in the case of multipass welding of thick plates of 304L stainless steel, chamfered in V shape, filled with two different wires.

Acknowledgements

This study was financially supported by the PERFORM program from the IRT Jules Verne. We acknowledge ILL (Grenoble, France) for the provision of experimental facilities. Parts of this

research were carried out at SALSA through the beam time allocated for proposal 1-02-337. We also acknowledge Renaud Frappier and his team from MAT-IN-MECA company (Sainte-Cécile, France) for the determination of longitudinal residual stress in the 1 – 100% 304L part with the contour method.

Declaration of Competing Interest

The authors declare that they have no competing financial interests or personal relationships that could have appeared to influence the work reported in this paper.

Bibliography

[1] W. Robert, J. Messler, I. The process and processes of welding, in: Principles of Welding: Processes, Physics, Chemistry, and Metallurgy, WILEY-VCH, 1999: pp. 3–123. https://doi.org/10.1002/9783527617487.

[2] W. Robert, J. Messler, II. The physics of welding, in: Principles of Welding: Processes, Physics, Chemistry, and Metallurgy, WILEY-VCH, 1999: pp. 127–312. https://doi.org/10.1002/9783527617487.

[3] A. Pavan, B. Arivazhagan, M. Vasudevan, S. Govind Kumar, Numerical simulation and validation of residual stresses and distortion in type 316L(N) stainless steel weld joints fabricated by advanced welding techniques, CIRP Journal of Manufacturing Science and Technology. 39 (2022) 294–307. https://doi.org/10.1016/j.cirpj.2022.08.010.

[4] S. Kou, 5. Residual Stresses, Distortion, and Fatigue, in: Welding Metallurgy, John Wiley & Sons, Ltd, 2002: pp. 122–141. https://doi.org/10.1002/0471434027.ch5.

[5] H.E. Coules, Contemporary approaches to reducing weld induced residual stress, Materials Science and Technology. 29 (2013) 4–18. https://doi.org/10.1179/1743284712Y.0000000106.

[6] A. Joseph, P. Palanichamy, S.K. Rai, T. Jayakumar, B. Raj, Non-destructive measurement of residual stresses in carbon steel weld joints, Science and Technology of Welding and Joining. (1998). https://doi.org/10.1179/stw.1998.3.6.267.

[7] J.H. Root, C.E. Coleman, J.W. Bowden, M. Hayashi, Residual Stresses in Steel and Zirconium Weldments, Journal of Pressure Vessel Technology. 119 (1997) 137–141. https://doi.org/10.1115/1.2842274.

[8] R.V. Preston, H.R. Shercliff, P.J. Withers, S.D. Smith, Finite element modelling of tungsten inert gas welding of aluminium alloy 2024, Science and Technology of Welding and Joining. (2013). https://doi.org/10.1179/136217103225008937.

[9] P. Asadi, S. Alimohammadi, O. Kohantorabi, A. Fazli, M. Akbari, Effects of material type, preheating and weld pass number on residual stress of welded steel pipes by multi-pass TIG welding (C-Mn, SUS304, SUS316), Thermal Science and Engineering Progress. 16 (2020) 100462. https://doi.org/10.1016/j.tsep.2019.100462.

[10] Y.C. Lin, K.H. Lee, Effect of preheating on the residual stress in type 304 stainless steel weldment, Journal of Materials Processing Technology. 63 (1997) 797–801. https://doi.org/10.1016/S0924-0136(96)02727-6.

[11] J. Li, Q. Guan, Y.W. Shi, D.L. Guo, Stress and distortion mitigation technique for welding titanium alloy thin sheet, Science and Technology of Welding and Joining. 9 (2004) 451–458. https://doi.org/10.1179/136217104225021643.

[12] J. Altenkirch, A. Steuwer, P.J. Withers, S.W. Williams, M. Poad, S.W. Wen, Residual stress engineering in friction stir welds by roller tensioning, Science and Technology of Welding and Joining. 14 (2009) 185–192. https://doi.org/10.1179/136217108X388624.

[13] X. Cheng, J.W. Fisher, H.J. Prask, T. Gnäupel-Herold, B.T. Yen, S. Roy, Residual stress modification by post-weld treatment and its beneficial effect on fatigue strength of welded structures, International Journal of Fatigue. 25 (2003) 1259–1269. https://doi.org/10.1016/j.ijfatigue.2003.08.020.

[14] S. Aoki, T. Nishimura, T. Hiroi, Reduction method for residual stress of welded joint using random vibration, Nuclear Engineering and Design. 235 (2005) 1441–1445. https://doi.org/10.1016/j.nucengdes.2005.02.005.

[15] C. Walker, A theoretical review of the operation of vibratory stress relief with particular reference to the stabilization of large-scale fabrications, Journal of Materials: Design and Applications. 225 (2011) 195–204. https://doi.org/10.1177/0954420711402877.

[16] C.M. Sonsino, F. Müller, J. de Back, A.M. Gresnigt, Influence of Stress Relieving by Vibration on the Fatigue Behaviour of Welded Joints in Comparison to Post-Weld Heat Treatment, Fatigue & Fracture of Engineering Materials & Structures. 19 (1996) 703–708. https://doi.org/10.1111/j.1460-2695.1996.tb01315.x.

[17] J. Altenkirch, A. Steuwer, M.J. Peel, P.J. Withers, S.W. Williams, M. Poad, Mechanical Tensioning of High-Strength Aluminum Alloy Friction Stir Welds, Metall Mater Trans A. 39 (2008) 3246–3259. https://doi.org/10.1007/s11661-008-9668-1.

[18] Y. Ma, D. Cuiuri, N. Hoye, H. Li, Z. Pan, The effect of location on the microstructure and mechanical properties of titanium aluminides produced by additive layer manufacturing using in-situ alloying and gas tungsten arc welding, Materials Science and Engineering: A. 631 (2015) 230–240. https://doi.org/10.1016/j.msea.2015.02.051.

[19] J. Wang, Z. Pan, D. Cuiuri, H. Li, Phase constituent control and correlated properties of titanium aluminide intermetallic alloys through dual-wire arc additive manufacturing, Materials Letters. 242 (2019) 111–114. https://doi.org/10.1016/j.matlet.2019.01.112.

[20] X. Cai, B. Dong, X. Yin, S. Lin, C. Fan, C. Yang, Wire arc additive manufacturing of titanium aluminide alloys using two-wire TOP-TIG welding: Processing, microstructures, and mechanical properties, Additive Manufacturing. 35 (2020) 101344. https://doi.org/10.1016/j.addma.2020.101344.

[21] Z. Qi, B. Cong, B. Qi, H. Sun, G. Zhao, J. Ding, Microstructure and mechanical properties of double-wire + arc additively manufactured Al-Cu-Mg alloys, Journal of Materials Processing Technology. 255 (2018) 347–353. https://doi.org/10.1016/j.jmatprotec.2017.12.019.

[22] J. Wang, Z. Pan, Y. Wang, L. Wang, L. Su, D. Cuiuri, Y. Zhao, H. Li, Evolution of crystallographic orientation, precipitation, phase transformation and mechanical properties realized by enhancing deposition current for dual-wire arc additive manufactured Ni-rich NiTi alloy, Additive Manufacturing. 34 (2020) 101240. https://doi.org/10.1016/j.addma.2020.101240.

[23] C. Shen, Z. Pan, Y. Ma, D. Cuiuri, H. Li, Fabrication of iron-rich Fe–Al intermetallics using the wire-arc additive manufacturing process, Additive Manufacturing. 7 (2015) 20–26. https://doi.org/10.1016/j.addma.2015.06.001.

[24] C. Shen, Z. Pan, D. Cuiuri, J. Roberts, H. Li, Fabrication of Fe-FeAl Functionally Graded Material Using the Wire-Arc Additive Manufacturing Process, Metall Mater Trans B. 47 (2016) 763–772. https://doi.org/10.1007/s11663-015-0509-5.

[25] J. Wang, Z. Pan, L. Wang, L. Su, K. Carpenter, J. Wang, R. Wang, H. Li, In-situ dual wire arc additive manufacturing of NiTi-coating on Ti6Al4V alloys: Microstructure characterization and mechanical properties, Surface and Coatings Technology. 386 (2020) 125439. https://doi.org/10.1016/j.surfcoat.2020.125439.

[26] Y. Feng, B. Zhan, J. He, K. Wang, The double-wire feed and plasma arc additive manufacturing process for deposition in Cr-Ni stainless steel, Journal of Materials Processing Technology. 259 (2018) 206–215. https://doi.org/10.1016/j.jmatprotec.2018.04.040.

[27] A.E. Davis, C.I. Breheny, J. Fellowes, U. Nwankpa, F. Martina, J. Ding, T. Machry, P.B. Prangnell, Mechanical performance and microstructural characterisation of titanium alloy-alloy composites built by wire-arc additive manufacture, Materials Science and Engineering: A. 765 (2019) 138289. https://doi.org/10.1016/j.msea.2019.138289.

[28] K. Zhang, J. Xiong, Y. Ke, Effect of latter feeding wire on double-wire GTA-AM stainless steel: Materials and Manufacturing Processes: Vol 36, No 5, (2021). https://www.tandfonline.com/doi/abs/10.1080/10426914.2020.1843677.

[29] T.A. Rodrigues, F.W. Cipriano Farias, K. Zhang, A. Shamsolhodaei, J. Shen, N. Zhou, N. Schell, J. Capek, E. Polatidis, T.G. Santos, J.P. Oliveira, Wire and arc additive manufacturing of 316L stainless steel/Inconel 625 functionally graded material: development and characterization, Journal of Materials Research and Technology. 21 (2022) 237–251. https://doi.org/10.1016/j.jmrt.2022.08.169.

[30] J.C. Lippold, D.J. Kotecki, 1 Introduction, in: Welding Metallurgy and Weldability of Stainless Steels, 1st edition, Wiley-Interscience, Hoboken, NJ, 2005: pp. 1–7. https://doi.org/10.4236/msa.2011.210195.

[31] J.C. Lippold, D.J. Kotecki, 9 Dissimilar welding of stainless steels, in: Welding Metallurgy and Weldability of Stainless Steels, 1st edition, Wiley-Interscience, Hoboken, NJ, 2005: pp. 287–308. https://doi.org/10.4236/msa.2011.210195.

[32] ASM Handbook Committee, Properties and Selection: Irons, Steels, and High-Performance Alloys, 1990. https://doi.org/10.31399/asm.hb.v01.9781627081610.

[33] L. Guilmois, Modélisation thermo-mécanique et approche expérimentale d'une opération de fabrication additive arc-fil, Thèse de doctorat, Université de Nantes, 2021.

[34] B.D. Cullity, in: Elements of X-Ray Diffraction, Addison-Wesley Publishing Company, 1978. https://doi.org/10.1119/1.1934486.

[35] V. Hauk, 2. X-ray diffraction, in: Structural and Residual Stress Analysis by Nondestructive Methods: Evaluation - Application - Assessment, Elsevier, 1997: pp. 17–494. https://doi.org/10.1016/B978-0-444-82476-9.X5000-2.

[36] T. Pirling, G. Bruno, P.J. Withers, SALSA—A new instrument for strain imaging in engineering materials and components, Materials Science and Engineering: A. 437 (2006) 139–144. https://doi.org/10.1016/j.msea.2006.04.083.

[37] G.E. Totten, Handbook of Residual Stress and Deformation of Steel, ASM International, 2002.

[38] J. Lu, Chapter 5: X-ray Diffraction Method, in: Handbook of Measurement of Residual Stresses, Fairmont Press, 1996: pp. 71–131.

[39] M.E. Fitzpatrick, A. Lodini, eds., Analysis of Residual Stress by Diffraction using Neutron and Synchrotron Radiation, CRC Press, London, 2003. https://doi.org/10.1201/9780203608999.

[40] A. Baghdadchi, V.A. Hosseini, L. Karlsson, Identification and quantification of martensite in ferritic-austenitic stainless steels and welds, Journal of Materials Research and Technology. 15 (2021) 3610–3621. https://doi.org/10.1016/j.jmrt.2021.09.153.

[41] E.F. Rauch, M. Véron, Automated crystal orientation and phase mapping in TEM, Materials Characterization. 98 (2014) 1–9. https://doi.org/10.1016/j.matchar.2014.08.010.

[42] A.-C. Gaillot, V.A. Drits, B. Lanson, POLYMORPH AND POLYTYPE IDENTIFICATION FROM INDIVIDUAL MICA PARTICLES USING SELECTED AREA ELECTRON DIFFRACTION, Clays Clay Miner. 68 (2020) 334–346. https://doi.org/10.1007/s42860-020-00075-9.

[43] P.-J. Yu, C.-Y. Huang, Y.-T. Lin, Y.-C. Su, H.-W. Yen, C.-A. Hsu, S.-H. Wang, J.-W. Yeh, W.-H. Hou, T.-R. Lin, T.-W. Hsu, Crystalline characteristics of a dual-phase precipitation hardening stainless steel in quenched solid solution and aging treatments, Materials Chemistry and Physics. 280 (2022) 125804. https://doi.org/10.1016/j.matchemphys.2022.125804.

[44] A. Schaeffler, Constitution Diagram for Stainless Steel Weld Metal, Metal Progress. 56 (1949) 680.

[45] F. Hosseinzadeh, J. Kowal, P.J. Bouchard, Towards good practice guidelines for the contour method of residual stress measurement, The Journal of Engineering. 2014 (2014) 453–468. https://doi.org/10.1049/joe.2014.0134.

[46] A. Jacob, J. Oliveira, A. Mehmanparast, F. Hosseinzadeh, J. Kelleher, F. Berto, Residual stress measurements in offshore wind monopile weldments using neutron diffraction technique

and contour method, Theoretical and Applied Fracture Mechanics. 96 (2018) 418–427. https://doi.org/10.1016/j.tafmec.2018.06.001.

[47] R.J. Katemi, J. Epp, F. Hoffmann, M. Steinbacher, Investigations of Residual Stress Distributions in Retained Austenite and Martensite after Carbonitriding of a Low Alloy Steel, Advanced Materials Research. 996 (2014) 550–555. https://doi.org/10.4028/www.scientific.net/AMR.996.550.

[48] C. Payares-Asprino, Effect of Martensite Start and Finish Temperature on Residual Stress Development in Structural Steel Welds, (n.d.). https://www.academia.edu/26063358/Effect_of_Martensite_Start_and_Finish_Temperature_on_Residual_Stress_Development_in_Structural_Steel_Welds (accessed March 5, 2023).